Absorber and phase defect inspection on EUV reticles using RESCAN

Iacopo Mochi, Sara Fernandez, Ricarda Nebling, Uldis Locans, Patrick Helfenstein, Rajendran Rajeev, Atoosa Dejkameh, Dimitrios Kazazis, Li-Ting Tseng, and Yasin Ekinci

Paul Scherrer Institute, Villigen, Switzerland

ABSTRACT

Reliable photomask metrology is required to reduce the risk of yield loss in the semiconductor manufacturing process. Actinic pattern inspection (API) of EUV reticles is a challenging problem to tackle with a conventional approach. For this reason we developed an API platform based on coherent diffraction imaging.

Aim: We want to verify the sensitivity of our platform to absorber and phase defects.

Approach: We designed and manufactured two EUV mask samples with absorber and phase defects and we inspected them with RESCAN in die-to-database mode.

Results: We reconstructed an image of an array of programmed absorber defects and we created a defect map of our sample. We inspected two programmed phase defect samples with buried structures of 3.5 nm and 7.8 nm height.

Conclusions: We verified that RESCAN in its current configuration can detect absorber defects in random patterns and buried (phase) defects down to 50×50 nm^2.

Keywords: EUV, actinic pattern inspection, phase defects, pellicle, lensless microscopy.

1. INTRODUCTION

Although the infrastructure for the insertion of extreme ultraviolet lithography (EUVL) into semiconductor high volume manufacturing is almost ready, actinic pattern inspection is still not available, exposing the risk of yield loss due to the presence of defects on the reticle. Our reflective-mode EUV mask scanning lensless imaging microscope (RESCAN) is an actinic pattern inspection platform currently under development at the Paul Scherrer Institute with the goal to enable defect inspection on EUV reticles for current and future lithography nodes.[1] RESCAN can operate in die-to-die or die-to-database mode by comparing the images of subsequent regions of the reticle with a reference and detecting the defects by evaluating differences in the signals.[2] RESCAN is based on coherent diffraction imaging (CDI). For this reason, it does not need complex and expensive EUV optics and it is capable of measuring the phase of the sample as well as its magnitude. The absence of optical elements in close proximity to the sample makes it possible to inspect reticles protected by EUV pellicles[3,4] which is a requirement for any mask inspection tool that has to be integrated into the lithography process.

1.1 RESCAN working principle and layout

RESCAN is a lensless microscope dedicated to EUV lithography mask inspection installed at the Swiss Light Source. The microscope has a dedicated beamline equipped with a tunable undulator and a monochromator with a bandwidth $\lambda/\Delta\lambda = 1500$. RESCAN's optical layout is illustrated in figure 1. The beam entering the RESCAN chamber has a numerical aperture $\mathrm{NA}_0 \simeq$ 5e-4 and is clipped by a selectable circular aperture with a diameter ranging from 0.2 mm to 4 mm. The beam is then focused onto the sample by a multilayer-coated toroidal mirror with a focal length of 120 mm. The angle of incidence of the beam on the sample is 6°. The illumination NA value ranges therefore between 1.7e-2 to 1.7e-3. The beam reflected and diffracted by the sample is collected by a 2048×2048 pixel CCD with a pixel size of 13.5 µm at a distance of 62 mm from the sample.

Further author information: (Send correspondence to Iacopo Mochi)

Iacopo Mochi: E-mail: Iacopo.Mochi@psi.ch

Extreme Ultraviolet (EUV) Lithography X, edited by Kenneth A. Goldberg, Proc. of SPIE Vol. 10957, 109570W · © 2019 SPIE · CCC code: 0277-786X/19/$18 · doi: 10.1117/12.2515160

Downloaded From: https://www.spiedigitallibrary.org/conference-proceedings-of-spie on 02 Oct 2019
Terms of Use: https://www.spiedigitallibrary.org/terms-of-use

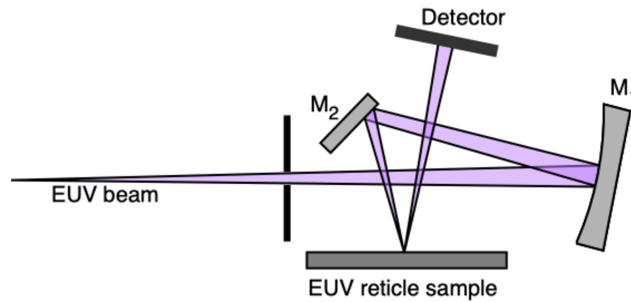

Figure 1. Schematic optical layout of RESCAN. The EUV beam comes from a dedicated beamline at the Swiss Light Source. The light is focused by a multilayer-coated toroidal mirror (M1) and folded onto the sample by a flat mirror (M2). The beam incidence angle on the EUV reticle sample is 6°.

RESCAN is based on ptychography,[5–7] a CDI technique that consists in scanning a sample with a coherent probe allowing some degree of overlap between the illuminated regions. The diffraction patterns are recorded with a pixel detector and used to retrieve a consistent estimate of the complex amplitude of the sample under investigation. As in other CDI approaches, when the diffraction pattern is recorded, the phase information is lost and it must be retrieved to reconstruct the sample image. In ptychography, the phase is obtained from the information redundancy generated by the overlapping of the illuminated regions.

Defect detection in RESCAN is performed comparing the reconstructed image to a reference one obtained from a control region (die-to-die) or calculated from the mask design (die-to-database) properly aligned and scaled to match the inspected area. A threshold is applied to the difference between the two images to avoid false positives that may arise from artifacts in the reconstruction or from the reference aerial image calculation. We have demonstrated that RESCAN is capable to detect programmed defects on EUV logic patterns using die-to-die and die-to-database approaches[2] and we tested it on pellicle-covered samples, evaluating the impact of different types of pellicles on the image quality.[8] We describe here the experiments performed in order to evaluate the inspection sensitivity of RESCAN for absorber and phase defects.

2. ABSORBER DEFECTS INSPECTION

The theoretical imaging resolution r of RESCAN in the configuration described in the previous section, is given by:

$$r = 0.61 \frac{\lambda}{\mathrm{NA}} = 0.61 \frac{13.5\ \mathrm{nm} \cdot 62\ \mathrm{mm}}{1024 \cdot 13.5\ \mathrm{\mu m}} = 37\ \mathrm{nm}. \tag{1}$$

To verify the sensitivity of RESCAN to absorber defects, we designed a sample layout with random structures with a critical dimension (CD) of 200 nm. The sample design includes a control structure with and without programmed intrusion, extrusion and pin-dot defects as shown in figure 2. The programmed defect structure is replicated in a 3×3 array with defect sizes from 200 nm to 20 nm. The layout was printed using e-beam lithography (EBL) on a multilayer-coated silicon wafer with a 140 nm thick hydrogen silsesquioxane (HSQ) absorber layer. The choice of HSQ as absorber was motivated by the availability of a stable and reliable, in-house lithography process for this material as opposed to other, better performing, absorber stacks like TaBN or nickel alloys.[9] The quality of the printed pattern was verified with scanning electron microscope (SEM) imaging down to a resolution of 50 nm.

We inspected the sample with RESCAN over a $30 \times 30\ \mathrm{\mu m}^2$ area centered on the array of programmed defect structures. The image detail containing the defect array is shown in figure 3A. We calculated the reference aerial image shown in figure 3B, starting from a mask design version without programmed defects. Assuming a plane wave illumination, we propagated the mask through a perfect lens with pupil shape and NA matching the ones defined by the RESCAN detector and a magnification of one. The intensity of the obtained aerial image was then scaled to match the one of the reconstructed image. The absolute value of the difference of the two images constitutes the sample's defect map. To limit the presence of false positives, a threshold was applied to the defect

Downloaded From: https://www.spiedigitallibrary.org/conference-proceedings-of-spie on 02 Oct 2019
Terms of Use: https://www.spiedigitallibrary.org/terms-of-use

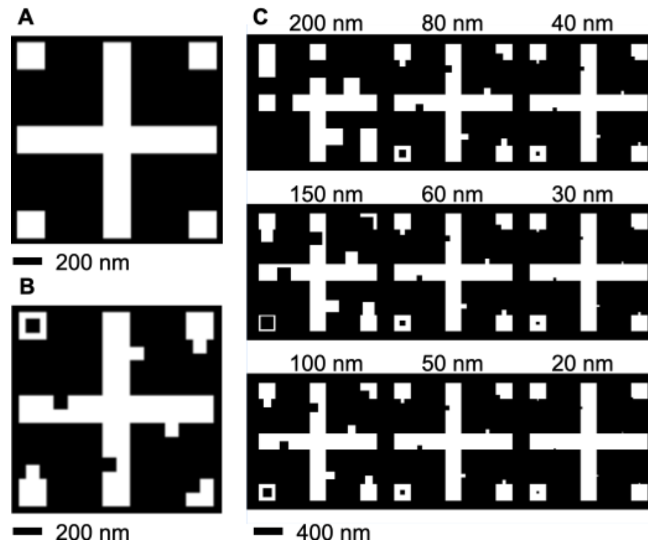

Figure 2. A: Control structure. B: Defect arrangement on the control structure. C: Matrix layout of the defective controlled structure. This matrix is embedded in a 26 × 26 µm random pattern area with 200 nm CD.

map. False positive signals are mainly caused by the oversimplified model used to calculate the reference image that doesn't take into consideration the 3D structure of the sample, the angle of incidence of the illumination and the optical properties of the absorber and the multilayer. In this kind of experiment, imperfections in the sample manufacturing with size comparable to the programmed defects, could also be detected as false positives, pending a more accurate verification of the sample structure. In this case, we choose a threshold of 50% on the defect map intensity that seems to account for the majority of the spurious signals. The thresholded defect map is shown in color, superimposed to the reconstructed image in figure 3C.

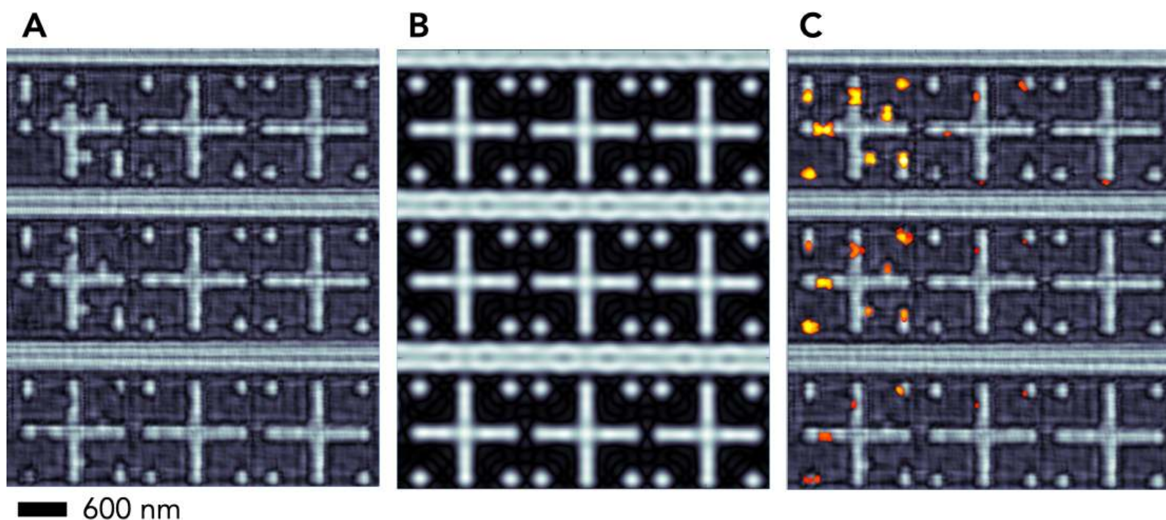

Figure 3. A: Detail of the sample image reconstructed with RESCAN featuring the matrix of control structures with programmed defects. B: Aerial image calculated from a version of the sample layout with defect-free control structures. C: The defect map calculated as the absolute value of the difference between the intensities of A and B is shown in color, superimposed to the reconstructed image A.

The single images of the detected defects are shown in figure 4 where it can be observed that line intrusions

Downloaded From: https://www.spiedigitallibrary.org/conference-proceedings-of-spie on 02 Oct 2019
Terms of Use: https://www.spiedigitallibrary.org/terms-of-use

(A) and corner intrusions (B) are detected down to a size of 50 nm, while pin-dot defects (C) and line extrusions (D) are detected down to 100 nm and 150 nm size respectively.

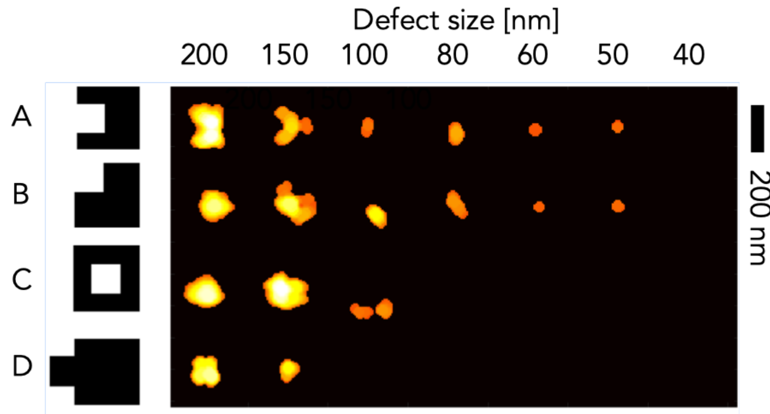

Figure 4. The single images of the defects shown in the map of figure 3C are arranged here in an array as a function of defect type and size. A: Line intrusion defects, detected down to a size of 50 nm. B: Corner intrusion defects, detected down to a size of 50 nm. C: Pin-dot defects, detected down to a size of 100 nm. D: Line extrusion defects, detected down to a size of 150 nm.

3. PHASE DEFECT INSPECTION

One of the advantages of CDI compared to standard imaging techniques is that from the complex amplitude of the reconstructed object, it is possible to measure the phase as well as the magnitude with a 2D scan of the object. This is of particular interest in the context of EUV mask inspection, where defects buried under or within the multilayer can create significant artifacts in the aerial images. These defects, often undetectable with SEM, AFM or DUV imaging,[10] can be investigated effectively with RESCAN. To evaluate the sensitivity of RESCAN to phase defects, we created a sample with programmed structures buried under the multilayer. The buried structures were defined by EBL on a silicon wafer spin-coated with PMMA resist. Then, a thin layer of carbon was deposited and the patterns were revealed by a lift-off process. We repeated this process on two samples with different carbon thickness (7.8 nm and 3.5 nm) and we verified the resulting structures profile with atomic force microscopy (AFM) as shown in figure 5. The AFM scan confirmed that the thickness values of the carbon layer were correct, but showed also that the liftoff process failed to remove some carbon on the edges of the structures. This effect can be prevented by increasing the thickness of the PMMA resist or by using a bilayer resist in order to facilitate the lift-off process. The samples were then coated with a MoSi multilayer with 40 bi-layers and a 64% EUV reflectance at 6º incidence.

The samples were finally coated with a 140 nm HSQ layer and patterned with e-beam lithography. The resulting sample layout is shown in figure 6, where the absorber pattern is represented in black and the buried structures are stippled with red lines. Among the carbon structures we generated, we included an array of 200 nm diameter dots with a pitch of 2 µm and we aligned a random logic-like absorber pattern on top of it. The absorber pattern has a CD of 200 nm and horizontal trenches (power rails) with a width of 400 nm. The trenches were aligned to the carbon dots in order to have phase structures on a clear region of the sample.

A detail of this arrangement is shown in figure 7 where we also included a SEM micrograph of the same region. In the SEM image, the contours of the defects are visible because of the extra carbon left by the liftoff process, but the buried structures are otherwise undetected.

We inspected the sample with 3.5 nm thick carbon structures in RESCAN and we extracted the phase and the magnitude from the measured complex amplitude. The contour of the buried defects is clearly visible in the magnitude image (Fig. 8A), but, more interestingly, the defects phase signature is also detected with good

Downloaded From: https://www.spiedigitallibrary.org/conference-proceedings-of-spie on 02 Oct 2019
Terms of Use: https://www.spiedigitallibrary.org/terms-of-use

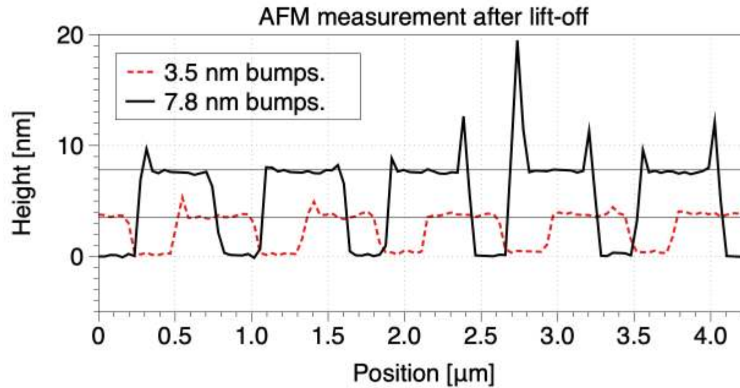

Figure 5. AFM profile scan of 500 nm wide carbon structures on two different samples. The profile scan confirms that the thickness values of the carbon structures are 3.5 nm and 7.8 nm. It also shows that the lift-off process failed to remove some carbon at the edges of the structures.

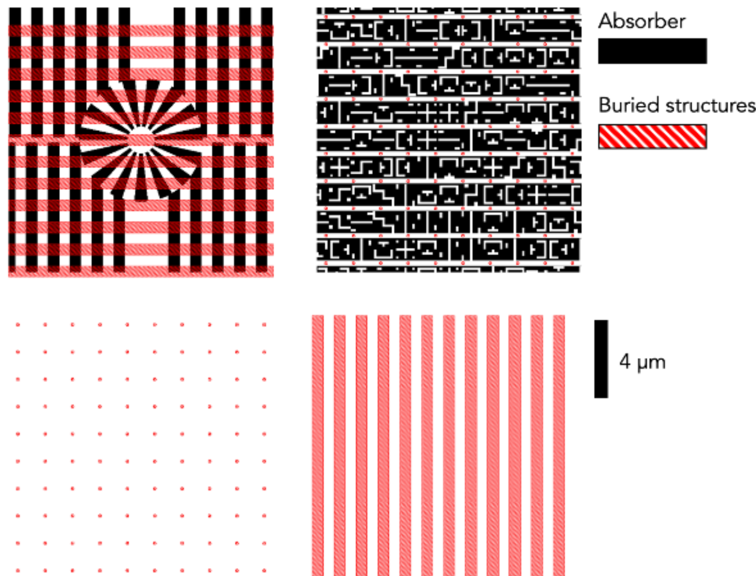

Figure 6. Detail of the sample layout including carbon buried structures and HSQ aborber pattern. The carbon structures consists of 800 nm wide lines and dots with 200 nm diameter and 2 µm pitch. The absorber pattern includes a Siemens star, an array of 800 nm wide lines and a random, logic-like field with 200 nm CD.

contrast in the phase map (Fig. 8B). If we model these structures as 3.5 nm bumps on a perfect mirror, we can estimate the phase difference from the flat region of the multilayer as:

$$\Delta\phi = \frac{4h\pi}{\lambda \cos\theta}, \tag{2}$$

where h is the bump height, λ is the wavelength and θ is the illumination angle of incidence. In this case we would expect $\Delta\phi = 1.05\pi$. The average phase difference for the carbon bumps shown in figure 8B is $\overline{\Delta\phi} = (0.93 \pm 0.05)\pi$. The difference between the measured and the estimated value could be explained by the fact that the model described by equation 2 underestimates the phase difference since it does not take into account the propagation through the multilayer.

We tested the 7.8 nm high structures on an absorber-free region with an array of phase contacts with 50 nm diameter and 2 µm pitch. The reconstructed magnitude and phase maps are shown in figure 9A and

Downloaded From: https://www.spiedigitallibrary.org/conference-proceedings-of-spie on 02 Oct 2019
Terms of Use: https://www.spiedigitallibrary.org/terms-of-use

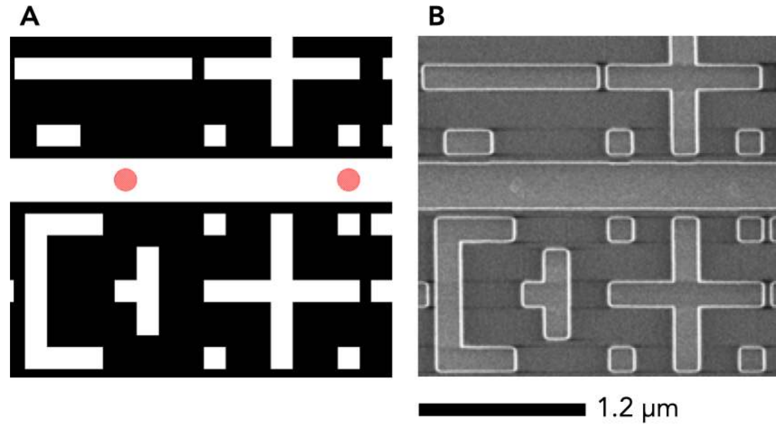

Figure 7. Detail of the random logic-like pattern shown in figure 6. A: The 200 nm carbon dots have been aligned to the horizontal 400 nm power rails in the pattern. B: SEM micrograph of the region shown in A with 7.8 nm carbon structures. The edges of the buried structures are barely visible because of the extra carbon left by the liftoff process. The central part of the dots was not detected by the SEM.

9B respectively. Even in this case, the defects are visible in the magnitude map, but their phase contrast is considerably lower than the previous case. Using equation 2, we obtain an estimated phase difference $\Delta\phi = 2.34\pi$, but since we measure the phase modulus 2π, we can expect to observe a phase difference of 0.34π. In this case though, the defect size is 50 nm, four times smaller than before and the propagation of the beam through the multilayer can't be neglected. Most of the bump is smoothed out by the multilayer deposition which explains why the average phase difference measured from the defects in image 9B is actually $\overline{\Delta\phi} = (0.13 \pm 0.02)\pi$.

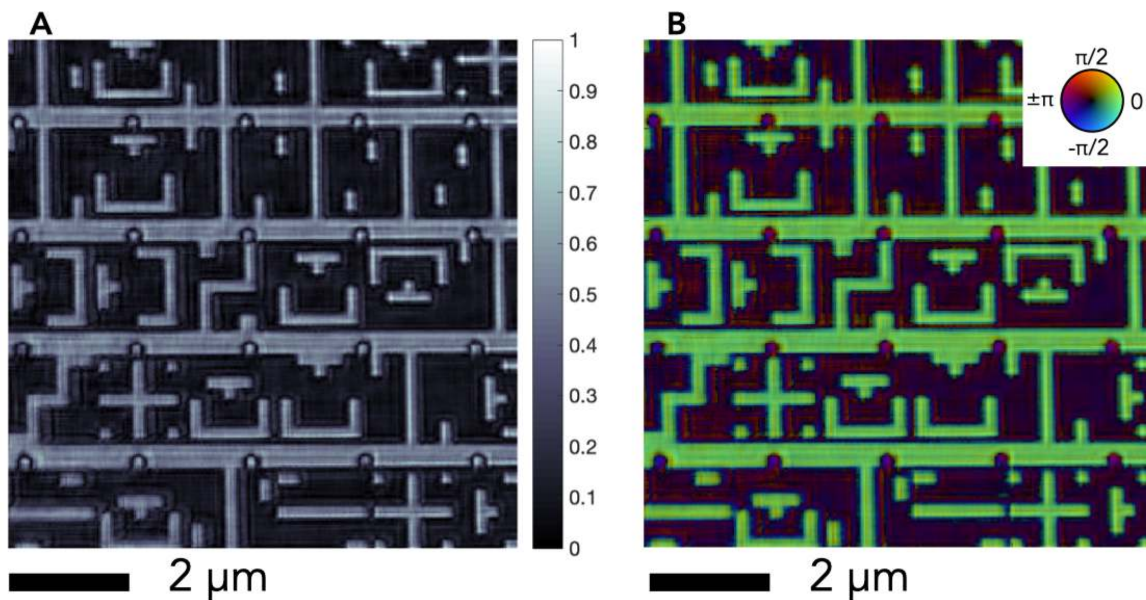

Figure 8. Detail of the reconstructed image of the sample with 3.5-nm high carbon structures. A: Reconstructed magnitude map. B. Reconstructed phase map.

Downloaded From: https://www.spiedigitallibrary.org/conference-proceedings-of-spie on 02 Oct 2019
Terms of Use: https://www.spiedigitallibrary.org/terms-of-use

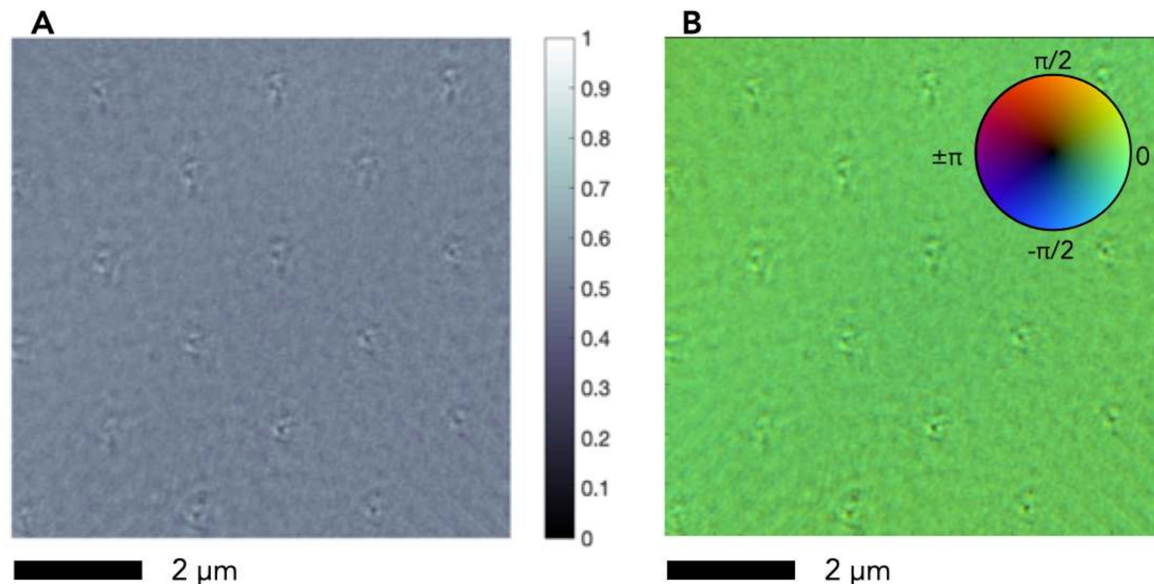

Figure 9. Detail of the reconstructed image of the sample with 7.5-nm high carbon structures. This area of the sample is absorber-free and under the multilayer there is an array of carbon dots with a diameter of 50 nm and a pitch of 2 µm. A: Reconstructed magnitude map. B. Reconstructed phase map.

4. CONCLUSIONS AND FUTURE PLANS

The RESCAN actinic pattern inspection microscope is a research and development platform for EUV mask inspection based on lensless imaging. After demonstrating the feasibility of actinic pattern inspection in die-to-die and in die-to-database mode,[2] and the ability of the microscope to inspect samples equipped with EUV pellicles,[8] we wanted to test the current defect sensitivity of RESCAN for absorber and buried structures. To investigate RESCAN's sensitivity to absorber defects, we fabricated a sample consisting of a multilayer-coated silicon wafer and a 140-nm thick HSQ absorber layer. We used e-beam lithography to pattern a random logic-like layout with a series of absorber defects of different type and size. Inspecting the sample with RESCAN, we generated a defect map that shows line intrusion and corner defects as small as 50×50 nm^2. To verify the ultimate resolution of the current configuration of RESCAN, a thorough verification of the defect's size on the sample with SEM imaging will have to be carried out. This verification will allow us to unbias the RESCAN results for structures smaller than 50 nm for which the printed dimensions may differ significantly from the pattern design layout.

We also tested the sensitivity of RESCAN to buried defects. For this purpose, we fabricated two test samples containing phase defects generated by carbon structures buried under the multilayer. We used carbon bumps of 3.5 nm and 7.8 nm. We used the complex amplitude of the images reconstructed with RESCAN to generate magnitude and phase maps of the samples and we observed that we can detect phase defects on clear and patterned regions. The smallest defects available on the test sample are 50 nm diameter dots and we were able to detect them both in the magnitude and in the phase domain. We also verified that 3.5 nm high buried structures generate phase disturbance close to the value expected from a simple model. For a verification of the phase reconstruction accuracy in RESCAN, we plan to perform an accurate modelling of the propagation of the beam through the multilayer in the presence of buried structures and compare the simulation results with RESCAN measurements.

ACKNOWLEDGMENTS

The authors wish to acknowledge the contribution of the technical support team at PSI, Michaela Vockenhuber, Markus Kropf and Josè Gabadinho, and thank OptixFab for providing the multilayer deposition on the test samples.

Downloaded From: https://www.spiedigitallibrary.org/conference-proceedings-of-spie on 02 Oct 2019
Terms of Use: https://www.spiedigitallibrary.org/terms-of-use

This project has received funding from the Electronic Component Systems for European Leadership Joint Undertaking under grant agreement No 783247-TAPES3. This Joint Undertaking receives support from the European Union's Horizon 2020 research and innovation program and Netherlands, Belgium, France, Germany, Israel.

REFERENCES

[1] Mochi, I., Helfenstein, P., Rajeev, R., Fernandez, S., Kazazis, D., Yoshitake, S., and Ekinci, Y., "Actinic inspection of EUV reticles with arbitrary pattern design," in [*International Conference on Extreme Ultraviolet Lithography: Photomask Technology and EUV Lithography*], *Proc.SPIE* **10450**, 1045007–1045016 (2017). [doi:10.1117/12.2280528].

[2] Mochi, I., Helfenstein, P., Mohacsi, I., Rajendran, R., Kazazis, D., Yoshitake, S., and Ekinci, Y., "RESCAN: an actinic lensless microscope for defect inspection of EUV reticles," *Journal of Micro/Nanolithography, MEMS, and MOEMS* **16** (2017). [doi:10.1117/1.JMM.16.4.041003].

[3] Gallagher, E., Timmermans, M. Y., Pollentier, I., Lee, J., Mariano, M., Adelmann, C., Huyghebaert, C., Scholze, F., and Laubis, C., "CNTs in the context of EUV pellicle history," in [*Advanced Lithography : Extreme Ultraviolet (EUV) Lithography IX*], *Proc.SPIE* **10583**, 105831E (2018). [doi:10.1117/12.2297710].

[4] Timmermans, M. Y., Mariano, M., Pollentier, I., Richard, O., C, H., and Gallagher, E. E., "Free-standing carbon nanotube films for extreme ultraviolet pellicle application," *Journal of Micro/Nanolithography, MEMS, and MOEMS* **17** (2018). [doi:10.1117/1.JMM.17.4.043504].

[5] Helfenstein, P., Rajeev, R., Mochi, I., Kleibert, A., Vaz, C. A. F., and Ekinci, Y., "Beam drift and partial probe coherence effects in EUV reflective-mode coherent diffractive imaging," *Opt. Express* **26**, 12242–12256 (Apr 2018). [doi:10.1364/OE.26.012242].

[6] Kewish, C. M., Thibault, P., Dierolf, M., Bunk, O., Menzel, A., Vila-Comamala, J., Jefimovs, K., and Pfeiffer, F., "Ptychographic characterization of the wavefield in the focus of reflective hard X-ray optics," *Ultramicroscopy* **110**(4), 325 – 329 (2010). [doi:10.1016/j.ultramic.2010.01.004].

[7] Harada, T., Kishimoto, J., Watanabe, T., Kinoshita, H., and Lee, D., "Mask observation results using a coherent extreme ultraviolet scattering microscope at NewSUBARU," *Journal of Vacuum Science & Technology B: Microelectronics and Nanometer Structures Processing, Measurement, and Phenomena* **27**(6), 3203–3207 (2009). [doi:10.1116/1.3258633].

[8] Mochi, I., Timmermans, M., Gallagher, E., Juste, M. M., Pollentier, I., Rajeev, R., Helfenstein, P., Fernandez, S., Kazazis, D., and Ekinci, Y., "Experimental evaluation of the impact of EUV pellicles on reticle imaging," *Proc.SPIE* **10810**, 10810 – 10819 (2018). [doi: 10.1117/12.2502480].

[9] Philipsen, V., Luong, K. V., Souriau, L., Erdmann, A., Xu, D., Evanschitzky, P., van de Kruijs, R. W. E., Edrisi, A., Scholze, F., Laubis, C., Irmscher, M., Naasz, S., Reuter, C., and Hendrickx, E., "Reducing extreme ultraviolet mask three-dimensional effects by alternative metal absorbers," *Journal of Micro/Nanolithography, MEMS, and MOEMS* **16**(4), 1 – 13 (2017). [doi:10.1117/1.JMM.16.4.041002].

[10] Mochi, I., Goldberg, K. A., La Fontaine, B., Tchikoulaeva, A., and Holfeld, C., "Actinic imaging of native and programmed defects on a full-field mask," *Proc.SPIE* **7636** (2010). [doi:10.1117/12.846670].

Downloaded From: https://www.spiedigitallibrary.org/conference-proceedings-of-spie on 02 Oct 2019
Terms of Use: https://www.spiedigitallibrary.org/terms-of-use